Journal of Physics B: Atomic, Molecular and Optical Physics

PAPER

Revealing the dissociation channels of mixed photons for H_2^+ in bicircularly polarized laser pulses

To cite this article: Pengkun Cao *et al* 2022 *J. Phys. B: At. Mol. Opt. Phys.* **55** 145601

IOP Publishing Journal of Physics B: Atomic, Molecular and Optical Physics
J. Phys. B: At. Mol. Opt. Phys. **55** (2022) 145601 (9pp) https://doi.org/10.1088/1361-6455/ac7270

Revealing the dissociation channels of mixed photons for H_2^+ in bicircularly polarized laser pulses

Pengkun Cao[1], Qingbin Zhang[1,*], Run Wang[1], Kunlong Liu[1,*] and Peixiang Lu[1,2]

[1] School of Physics and Wuhan National Laboratory for Optoelectronics, Huazhong University of Science and Technology, Wuhan 430074, People's Republic of China
[2] Optics Valley Laboratory, Hubei 430074, People's Republic of China

E-mail: zhangqingbin@hust.edu.cn and liukunlong@hust.edu.cn

Received 21 January 2022, revised 16 May 2022
Accepted for publication 22 May 2022
Published 10 June 2022

Abstract

We theoretically study the dissociation of H_2^+ driven by the bicircularly polarized (BiCP) laser pulses. It is shown that there is a possibility for the molecule dissociating through the mixed-photon channels, in which the system simultaneously absorbs multiple photons of different frequencies from the BiCP pulses. Setting the frequency ratios of 1 : 2 and 1 : 3 for the BiCP pulses reveals the mixed-photon dissociation channels from the interference patterns in the angle-resolved kinetic energy spectra. In addition, by applying the wave packet interference approach, we show that one can further estimate the fragment yield ratios between different dissociation channels that lead to the same kinetic energy.

Keywords: multiple photon dissociation, dissociation channel, wave packet interference

(Some figures may appear in colour only in the online journal)

1. Introduction

Laser-driven dissociation of molecules is one of the most interesting research areas in strong-field physics. Understanding the dynamics in laser-molecular interaction is the primary step toward controlling the formation and fracture of chemical bonds with laser fields [1–3]. Being the simplest molecule in nature, the hydrogen molecular ion H_2^+ plays a fundamental role in the theoretical and experimental studies of molecular dissociation in intense laser fields [4–7]. Previous studies show that, via adjusting the frequency, the intensity and the CEP of the laser pulses, the dissociation pathways of H_2^+ can be manipulated [8–12]. Among these studies, the linearly polarized (LP) laser pulses are usually applied to drive the dissociation of H_2^+. Recent studies [13, 14] show that the dissociation of H_2^+ in circularly polarized (CP) laser pulses exhibits different features from those in LP laser pulses. For example, Chen *et al* found the spiral interference patterns in the nuclear momentum distributions due to the interference of different dissociation pathways in the two sequential CP pulses with different wavelengths. It is shown [13, 14] that the underlying molecular dynamics can be revealed by analyzing the spiral structures of the nuclear momentum distributions. In their study, two CP pulses are well separated and, thus, only single-color photons are absorbed or emitted during the interaction with each pulse. In contrast, for two CP pulses overlapping in time, namely, bicircularly polarized (BiCP) pulses, the dissociation process becomes more interesting but complicated [15]. This paper aims to study the mixed-photon dissociation (MiPD) channels of H_2^+ driven by the counterrotating BiCP laser pulses. It was shown previously that the system would simultaneously absorb photons of different frequencies from the BiCP pulses and ends up with ionization [16, 17]. For molecular dissociation, therefore, it would be interesting to know how the MiPD channels take place during the interaction and how we can measure them. The MiPD channels potentially increase the possible dissociation pathways while some of them end up with the same kinetic energy release (KER). In order to identify different MiPD pathways, we propose an

* Authors to whom any correspondence should be addressed.

approach that combines the analysis of the KER and the angular momentum of the molecular fragments. We find symmetric angular distributions caused by the interference of the dissociation fragments from different pathways. Furthermore, we weigh the yield ratio of the coherent pathways by the contrast of interfering stripes. Finally, the wave packet interference using a delayed third CP pulse is proposed to identify the dominant MiPD pathway.

2. Numerical methods

The photodissociation process of H_2^+ is mainly governed by the $1s\sigma_g$ and $2p\sigma_u$ electronic states, which are energetically well separated from other higher states. Therefore, as long as the applied laser field is not too high ($\leqslant 10^{14}$ W cm^{-2}), the calculation based on the two-level model for H_2^+ yields reasonable results [13]. Here, we solve numerically the two-dimensional two-level time dependent Schrödinger equation (TDSE) [14] for H_2^+, which is written as (in the length gauge)

$$i\frac{\partial}{\partial t}\begin{bmatrix}\psi_g(R_x,R_y,t)\\ \psi_u(R_x,R_y,t)\end{bmatrix} = \begin{bmatrix}\frac{\hat{P}_x^2+\hat{P}_y^2}{2M}+V_g(R_x,R_y) & \mathbf{D}(R_x,R_y)\cdot\mathbf{E}(t)\\ \mathbf{D}(R_x,R_y)\cdot\mathbf{E}(t) & \frac{\hat{P}_x^2+\hat{P}_y^2}{2M}+V_u(R_x,R_y)\end{bmatrix} \times \begin{bmatrix}\psi_g(R_x,R_y,t)\\ \psi_u(R_x,R_y,t)\end{bmatrix}, \quad (1)$$

where V_g (R_x, R_y) and V_u (R_x, R_y) are the potential surface of the $1s\sigma_g$ and $2p\sigma_u$ states, respectively. $\mathbf{D}$ (R_x, R_y) is the transition dipole moment between two states. $\mathbf{E}(t)$ indicates the external electric field, which is given by

$$\mathbf{E}(t) = \mathbf{E}_1(t) + \mathbf{E}_2(t) \quad (2)$$

with

$$\mathbf{E}_1(t) = \mathcal{E}_1 \sin^2\left(\frac{\pi t}{L}\right)[\cos(\omega_1 t)\hat{x} - \sin(\omega_1 t)\hat{y}] \quad (3)$$

and

$$\mathbf{E}_2(t) = \mathcal{E}_2 \sin^2\left(\frac{\pi t}{L}\right)[\cos(\omega_2 t)\hat{x} \pm \sin(\omega_2 t)\hat{y}] \quad (4)$$

for $0 < t < L$. $\mathbf{E}_1(t)$ is the left circularly polarized laser pulse and $\mathbf{E}_2(t)$ is the left or right CP laser pulse. $\mathcal{E}_1$ and $\mathcal{E}_2$, ω_1 and ω_2, L are the field amplitudes, angular frequencies and the full duration of the two pulses, respectively. We have set the two pulses to the same pulse duration. In fact, the slight difference in laser pulse duration does not affect our conclusions.

In our simulations, the wave function is propagated in an 168 a.u. × 168 a.u. box with 2048 grids in each dimension. The time step is $\delta t = 0.2$ a.u. In the calculation we consider several different initial states of the nuclear wave packets. The first is the ground vibrational state of H_2^+, which has been applied in many studies [9, 18, 25]. The second is the vibrational state $v = 1, 2, 3$. When H_2^+ ion beam produced from a low-energy ion accelerator, the numerical simulations may start from the above different vibrational states of H_2^+ separately [19]. When H_2^+ are obtained by laser ionization, we have to consider the coherent superimposition of the different vibrational states. The third is the superimposed coherent state, which is composed of three vibrational state $v = 1, 2, 3$. These vibrational states are the three most distributed vibrational states after the ionization of H_2 by laser pulse [20]. The above vibrational state can be obtained by the imaginary-time propagation algorithm [21]. After the laser field is over, we keep propagating the wave function until the dissociative nuclear wave packet (NWP) reaches the region where $R > 20$ a.u., while the simulation box is large enough to avoid the reflection of the NWP at the boundary during the propagation. Finally, by filtering out the well-separated bound NWP, one can obtain the two-dimensional momentum distributions for the dissociative NWPs on the $1s\sigma_g$ and $2p\sigma_u$ potential surfaces, respectively, by applying the Fourier transformation. The angle-resolved KER distributions can also be obtained from the two-dimensional nuclear momentum distributions via coordinate transformation.

3. Scheme and results

3.1. Scheme and expression symbol

When the H_2^+ is exposed to the monochromatic laser pulse, it can dissociate along multiple pathways, as shown in figure 1(a). The typical pathways include the one-photon pathway, net-two-photon pathway and three-photon pathway, which have been extensively studied both theoretically and experimentally [22–24]. For example, by using the interference of the H^+ fragments from the three-photon pathway and the net-two-photon pathway, researchers have implemented electron localization [9, 25–27].

In the case of BiCP pulses, the MiPD pathway would take place, as shown in figure 1(b). The H_2^+ in the $1s\sigma_g$ state can be launched to the $2p\sigma_u$ curve by absorbing the photons of different frequencies. Different combinations of laser frequencies could lead to different dissociation pathways. In the present study, we will apply the BiCP laser pulses with the frequency ratios of 1 : 2 and 1 : 3. These frequency ratios are commonly used in experiments.

Firstly, we show in figures 2(a) and (b) the potential curves as well as the MiPD channels at some critical internuclear distances for the frequency ratios of $\omega_1 : \omega_2 = 1 : 3$ and $\omega_1 : \omega_2 = 1 : 2$, respectively. R_n represent internuclear distance at which the potential energy difference between the $1s\sigma_g$ curve and the $2p\sigma_u$ curve is equal to the energy of n photons with frequency ω_1. R_1 to R_5 are shown in the figure. Due to the opposite parity between the $1s\sigma_g$ and $2p\sigma_u$ states, H_2^+ in the $1s\sigma_g$ state can only absorb odd number of photons to be launched to the repulsive $2p\sigma_u$ curve. For the frequency ratio of $\omega_1 : \omega_2 = 1 : 2$, the transition can occur at R_i ($i = 5, 4, 3, 2, 1$), as shown in figure 2(b). For the frequency ratio of $\omega_1 : \omega_2 = 1 : 3$, the transition can only occur at R_1, R_3 and R_5, as shown in figure 2(a). Note that higher photon absorption is not considered here as the corresponding transition probabilities would be very low.

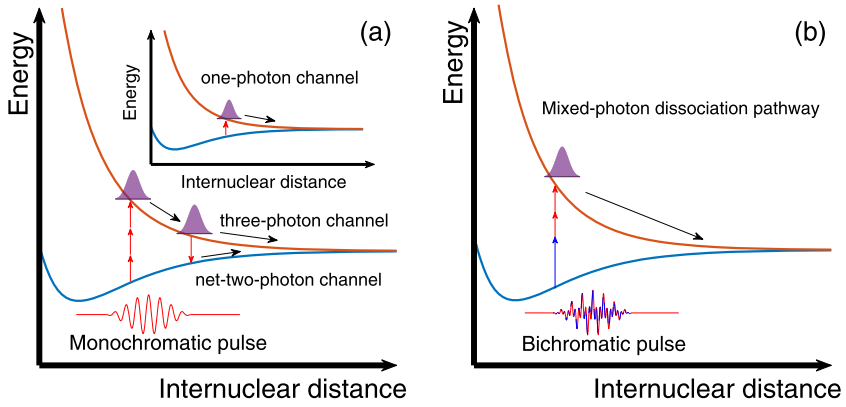

Figure 1. The sketch of typical dissociation pathways and MiPD pathway are shown in (a) and (b), respectively.

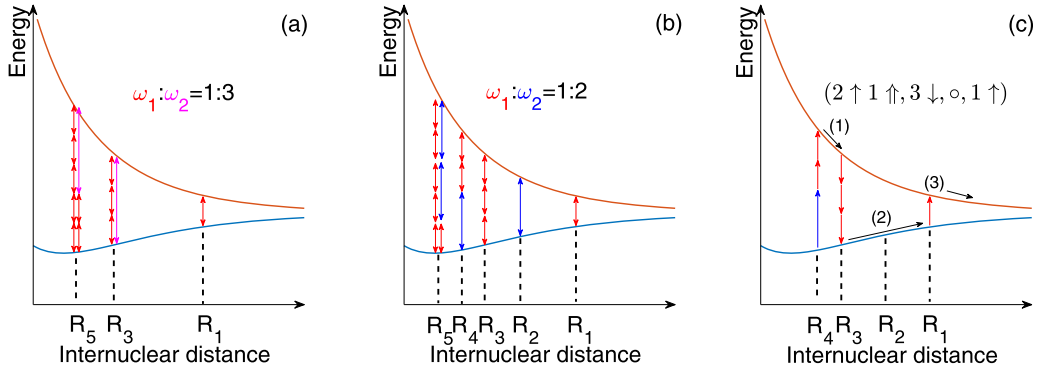

Figure 2. The potential curves and coupling regions for (a) $\omega_1 : \omega_2 = 1 : 3$ and (b) $\omega_1 : \omega_2 = 1 : 2$. The short and long double-head arrow represent absorbing or releasing photon of frequency ω_1 and photon of frequency ω_2. R_1 to R_5 represent the internuclear distance at which potential energy difference between $1s\sigma_g$ curve and $2p\sigma_u$ curve equals the energy of 1 to 5 photons with frequencies of ω_1. (c) An example of dissociation pathway. $\omega_1 : \omega_2 = 1 : 2$. R_1 to R_4 are the coupling regions. The short uparrow (downarrow) represent the NWP absorb (release) the photon with frequency of ω_1. The long uparrow (downarrow) represent the NWP absorb (release) the photon with frequency of ω_2. This dissociation pathway can be represented by $(2\uparrow 1\Uparrow, 3\downarrow, \circ, 1\uparrow)$.

Considering the coexistence of the monochromatic-photon dissociation channels and the MiPD ones, the dissociation pathways appear to be complex. To facilitate the description, we have defined the expressions for describe different dissociation pathways. We represent the pathways as $(A(R_n), A(R_{n-1}), \ldots, A(R_1))$, where $R_1, R_2, \ldots, R_n$ represent the first, second, …, nth coupling region. The value of n could be as large as desired, but in this paper, we only consider $n = 4$ for $\omega_1 : \omega_2 = 1 : 2$ and $n = 5$ for $\omega_1 : \omega_2 = 1 : 3$. $A(R_n)$ is a symbol, which represents the transition occurring at the coupling region R_n. The alternative symbols are $n\uparrow, n\Uparrow, n\downarrow$, and $n\Downarrow$ for $A(R_n)$. $n\uparrow$ ($n\downarrow$) and $n\Uparrow$ ($n\Downarrow$) represent the system absorbing (releasing) n photons of the frequency ω_1 and ω_2, respectively. In addition, the symbol '$\circ$' will be used to indicate the case that the NWP passes the critical internuclear distances without absorbing or releasing photons.

We illustrate the expressions with an example of a dissociation pathway. As shown in figure 2(c), the NWP is launched to the $2p\sigma_u$ curve at R_4 by absorbing one photon of ω_2 and two photons of ω_1 and then dropped at R_3 by emitting three photons of ω_1. Then, it passes R_2 and is launched again to the $2p\sigma_u$ curve by absorbing one photon of ω_1 at R_1. Such pathway can be expressed as $(2\uparrow 1\Uparrow, 3\downarrow, \circ, 1\uparrow)$.

Next, we perform a theoretical analysis of the dissociation pathways in the BiCP pulses. For the NWP from jth pathway, we can denote it as ψ_j, which can be expressed as [13]

$$\psi_j = A_j(K)\mathrm{e}^{\mathrm{i}[m_j\phi+\eta_j(K)]}, \tag{5}$$

where K is KER of dissociative fragment, $A_j(K)$ is the amplitude and $\eta_j(K)$ is a KER-dependent phase term. m_j is the angular momentum, which depends on the sum of angular momentum of the photons absorbed and released by the molecule during the interaction. We take the dissociation pathway in figure 2(c) as an example. We assume the laser pulse of frequency ω_1 is left-rotating carrying angular momentum of $+1$ and the laser pulse of frequency ω_2 is right-rotating carrying angular momentum of -1. Then, the operator $n\uparrow$ ($n\downarrow$) will change the angular momentum of NWP by $+1(-1)$, and $n\Uparrow$ ($n\Downarrow$) will change the angular momentum of NWP by $-1(+1)$. As shown in figure 2(c), the NWP initially absorbs two photons with the angular momentum of $+1$ and one photon with the angular momentum of -1. It carries an angular momentum of 1 at the location marked by (1). Then, after releasing three photons with the angular momentum of $+1$ at R_3, the angular momentum of the NWP becomes -2 at the location marked by (2). Finally, the NWP absorb one photon

with the angular momentum of 1 at R_1 and the angular momentum eventually becomes -1 at (3). So, the angular momentum m of the dissociative NWP is -1 for the dissociation pathway shown in figure 2(c).

When the dissociating fragments from two pathways end up with the same KER, they will interfere with each other. The interference structure in the angle-resolved KER distribution can be expressed as

$$\begin{aligned} P(K,\phi) &= |\psi_1+\psi_2|^2 \\ &= |A_1(K)e^{i[m_1\phi+\eta_1(K)]}+A_2(K)e^{i[m_2\phi+\eta_2(K)]}|^2 \\ &= |A_1(K)|^2+|A_2(K)|^2 \\ &\quad +2A_1(K)A_2(K)\cos(\Delta m\phi-\Delta\eta), \end{aligned} \tag{6}$$

where ψ_1 and ψ_2 represent the NWPs of two dissociation pathways, respectively and we have $\Delta m = m_1 - m_2$ and $\Delta\eta = \eta_1 - \eta_2$. The equation indicates that the interference pattern oscillates with ϕ in the period of $2\pi/\Delta m$. Thus, the final angular momenta of the NWPs can be extracted via analyzing the interference patterns. Moreover, the phase term $\Delta\eta$ contains the time information. By extracting the phase term $\Delta\eta$, one can further evaluate the time difference between the two pathways.

3.2. *Dissociation pathways with* $\omega_1 : \omega_2 = 1 : 3$

This subsection will consider the dissociation pathways in the BiCP pulses with $\omega_1 : \omega_2 = 1 : 3$. As shown in figure 2(a), there are three coupling regions where the NWP can be launched or dropped. In order to analyse the dissociation pathways, we list the KER and the angular momentum for all possible dissociation pathways in table 1. The wavelengths of the two pulses are 800 nm ($\omega_1 = 0.057$ a.u.) and 266 nm ($\omega_2 = 0.171$ a.u.), respectively. The KER in table 1 is estimated from the potential energy curve and the coupling region. m is obtained from the number and frequency of absorbed photons.

As shown in table 1, the $(3\uparrow, \circ, \circ)$ pathway and the $(1\Uparrow, \circ, \circ)$ pathway have the same KER, corresponding to the three-photon and one-photon dissociation pathways, respectively. There are four pathways which have the KER of 2.17 eV. The fragments from these pathways interfere with each other. Distinguishing these pathways is difficult. We mainly focus on the $(2\uparrow 1\Uparrow, \circ, \circ, \circ, \circ)$ $(5\uparrow, \circ, \circ, \circ, \circ)$ pathways. The dissociation fragments from the two pathways will generate interference pattern because of the same KER. When the laser pulses of the frequency ratio ω_1 and ω_2 are counter-rotating, the angular momenta m of the NWPs from $(2\uparrow 1\Uparrow, \circ, \circ, \circ, \circ)$ pathway and the $(5\uparrow, \circ, \circ, \circ, \circ)$ pathway are 1 and 5, respectively (we have assumed the laser pulse of ω_1 is left-handed rotation). Then, we will have $\Delta m = 4$, and the angular dissociation yield at the given KER will oscillate in the period of $2\pi/4$. If the laser pulses of frequency ω_1 and ω_2 are co-rotating, we will have $\Delta m = 2$, and the angular dissociation yield at the given KER will oscillate in the period of $2\pi/2$.

Next, we simulated the H_2^+ dissociation process in BiCP pulses using the TDSE method. The two laser pulses have been set to the appropriate intensity to ensure that the yield of dissociative fragments from different pathways is similar to produce a clear interference structure. The two-dimensional momentum distributions and the angle-resolved KER distributions for the dissociation of H_2^+ in the counter-rotating and co-rotating BiCP pulses with $\omega_1 : \omega_2 = 1 : 3$ are shown in figures 3(a)–(d), respectively.

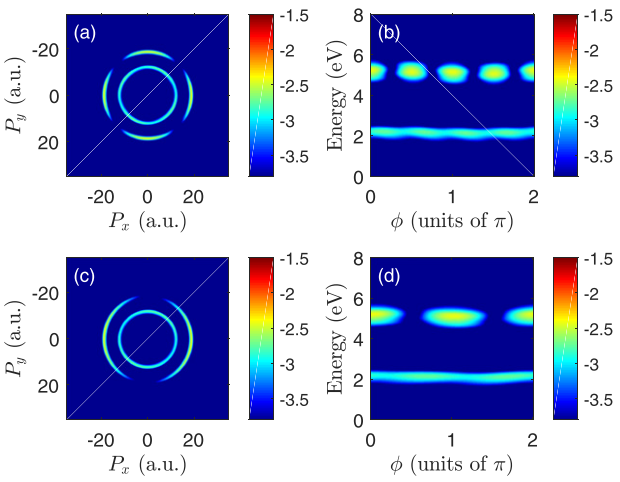

Figure 3. The two-dimension momentum distribution and angle-resolved KER distribution of H^+ fragments in the overlapped counter-rotating and co-rotating BiCP pulses with $\omega_1 : \omega_2 = 1 : 3$ are shown in (a), (b), (c) and (d), respectively. The wavelengths of $\mathbf{E}_1(t)$ and $\mathbf{E}_2(t)$ are 800 nm ($\omega_1 = 0.057$ a.u.) and 266 nm ($\omega_2 = 0.171$ a.u.), respectively. $L_1 = L_2 = 16.01$ fs. The intensity of $\mathbf{E}_1(t)$ and $\mathbf{E}_2(t)$ are 2.5×10^{13} W cm^{-2} in (a), (b), (c) and (d). The figures are logarithmic with the base of 10.

As shown in figures 3(b) and (d), the interference pattern appears around 5.28 eV in the angle-resolved KER spectra. The oscillating period along ϕ are $2\pi/4$ and $2\pi/2$ for the counter-rotating and co-rotating CP laser fields, respectively. This is consistent with our analysis above. The horizontal band around KER ≈ 2.17 eV is contributed by the four pathways with KER of 2.17 eV, as already given in table 1. We note that there are hardly fragments with the KER of 0.86 eV or 2.87 eV. This is because the ground-state wave packet are rarely distributed in the coupling region of R_1 and R_3.

Next, we calculated the results starting from the vibrational states $v = 1, 2, 3$ with counter-rotating BiCP pulses. The two-dimension momentum distribution and angle-resolved KER distribution are shown in the first row, second row and third row of figure 4, respectively. The symmetric structure with a period of $2\pi/4$ appears near 5.28 eV in the three results. In the low-energy region, the dissociative fragments have more yields starting from the excited vibrational states. This is due to that the excited vibrational state wave packets have more populations at larger nuclear distance.

The simulated result starting from coherent superimposed state are shown in figure 5. The interference structure of our interest at energies of about 5.28 eV is clear. This indicates that our MiPD pathways can be observed in different initial states.

To experimentally observe the phenomenon, we should first ionize H_2 with a CP laser pulse [14]. The H_2^+ would generate

Table 1. The dissociation pathways for $\omega_1 : \omega_2 = 1 : 3$ are listed in the first column. The calculated KER was listed in the second column. The third and fourth columns are angular momentum for counter-rotating and co-rotating laser pulses, respectively.

Pathway					KER (eV)	m (counter-rotating)	m(co-rotating)
$5\uparrow$	$\circ$	$\circ$	$\circ$	$\circ$	5.28	5	5
$2\uparrow 1\Uparrow$	$\circ$	$\circ$	$\circ$	$\circ$	5.28	1	3
$\circ$	$\circ$	$1\Uparrow$	$\circ$	$\circ$	2.87	-1	1
$\circ$	$\circ$	$3\uparrow$	$\circ$	$\circ$	2.87	3	3
$\circ$	$\circ$	$\circ$	$\circ$	$1\uparrow$	0.86	1	1
$5\uparrow$	$\circ$	$1\Downarrow$	$\circ$	$1\uparrow$	2.17	7	5
$5\uparrow$	$\circ$	$3\downarrow$	$\circ$	$1\uparrow$	2.17	3	3
$2\uparrow 1\Uparrow$	$\circ$	$1\Downarrow$	$\circ$	$1\uparrow$	2.17	3	3
$2\uparrow 1\Uparrow$	$\circ$	$3\downarrow$	$\circ$	$1\uparrow$	2.17	-1	1

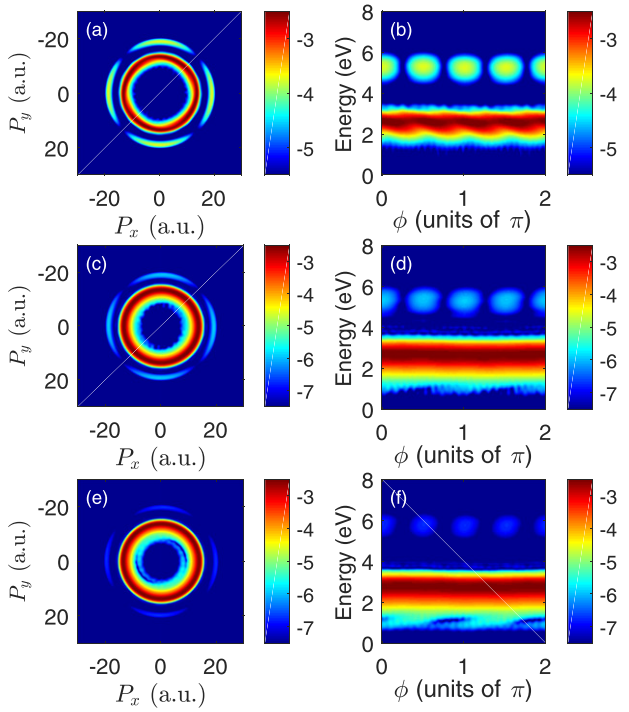

Figure 4. The two-dimension momentum distribution and angle-resolved KER distribution of H^+ fragments in the overlapped counter-rotating BiCP pulses with $\omega_1 : \omega_2 =$ 1:3 starting from vibrational state $v = 1$, $v = 2$, $v = 3$ are shown in the first row, second row and third row, respectively. The wavelengths of $\mathbf{E}_1(t)$ and $\mathbf{E}_2(t)$ are 800 nm ($\omega_1 = 0.057$ a.u.) and 266 nm ($\omega_2 = 0.171$ a.u.), respectively. $L_1 = L_2 = 16.01$ fs. The intensity of $\mathbf{E}_1(t)$ and $\mathbf{E}_2(t)$ are 2.5×10^{13} W cm^{-2}. The figures are logarithmic with the base of 10.

in the Franck–Condon region. And then we introduce a delay bicircularly laser pulses to dissociate the H_2^+. The momentum of dissociative fragments can be detected by velocity map imaging [28, 29] or cold target recoil ion momentum spectroscopy [30]. Note that the intensity of the laser pulses should be carefully adjusted to ensure that the fragment yields from different pathways have similar yields.

3.3. Dissociation pathways with $\omega_1 : \omega_2 = 1 : 2$

For the case of $\omega_1 : \omega_2 = 1 : 2$, we found that the pathways are more complex, because there are five coupling regions where

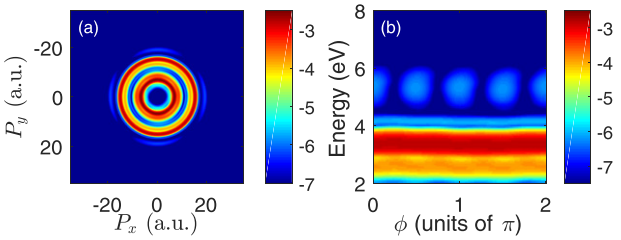

Figure 5. The two-dimension momentum distribution and angle-resolved KER distribution of H^+ fragments in the overlapped counter-rotating BiCP pulses with $\omega_1 : \omega_2 =$ 1:3 starting from superimposed coherent state. The wavelengths of $\mathbf{E}_1(t)$ and $\mathbf{E}_2(t)$ are 800 nm ($\omega_1 = 0.057$ a.u.) and 266 nm ($\omega_2 = 0.171$ a.u.), respectively. $L_1 = L_2 = 12.01$ fs. The intensity of $\mathbf{E}_1(t)$ and $\mathbf{E}_2(t)$ are 2.5×10^{13} W cm^{-2} and 2.5×10^{12} W cm^{-2}. The figures are logarithmic with the base of 10.

the resonant excitation can happen. This means the NWP may undergo multiple transition processes during the dissociation. Identifying the pathways would be pretty tricky if the NWP was launched to $2p\sigma_u$ curve at R_5. Therefore, we reduce the laser intensity appropriately so that the NWP can hardly be launched to the $2p\sigma_u$ curve at R_5. We list the pathways for $\omega_1 : \omega_2 = 1 : 2$ in table 2. The wavelengths of the two laser pulses are 600 nm ($\omega_1 = 0.076$ a.u.) and 300 nm ($\omega_1 = 0.152$ a.u.), respectively. We focus on the pathways of $(2\uparrow 1\Uparrow, 3\downarrow, 1\uparrow, \circ)$ and $(2\uparrow 1\Uparrow, \circ, 1\Downarrow, 1\uparrow)$, which share the close KER energies. Δm of these two pathways are 6 and 2 in the counter-rotating and co-rotating BiCP pulses, respectively.

The momentum distributions and the angle-resolved KER distributions are shown in figure 6. The first and second rows correspond to the counter-rotating and co-rotating BiCP pulses, respectively. For the first row in figure 6, $\mathbf{E}_1(t)$ is left-handed rotation and $\mathbf{E}_2(t)$ is right-handed rotation. And for the second row, both laser pulses are left-handed rotation.

The KER of the fragments distributes in two regions, around 5.7 eV and around 3.6 eV. No significant yield is found in the region higher than 6 eV, which means that our field intensity is weak enough to avoid the excitation of the NWP at around R_5. The fragments with KER of 5.7 eV are from the $(2\uparrow 1\Uparrow, \circ, \circ, \circ, \circ)$ pathway. Interference pattern appears around the KER of 3.6 eV and the oscillating period along ϕ are $2\pi/6$ and $2\pi/2$ in the counter-rotating and the co-rotating

Table 2. The pathways for $\omega_1 : \omega_2 = 1 : 2$ are listed in the first column. The calculated KER was listed in the second column. The third and fourth columns are angular momentum for counter-rotating and co-rotating laser pulses, respectively.

Pathway				KER (eV)	m(counter-rotating)	m(co-rotating)
$2\uparrow 1\Uparrow$	$\circ$	$\circ$	$\circ$	5.69	1	3
$\circ$	$3\uparrow$	$\circ$	$\circ$	4.01	3	3
$\circ$	$\circ$	$1\Uparrow$	$\circ$	2.50	-1	1
$\circ$	$\circ$	$\circ$	$1\uparrow$	1.17	1	1
$2\uparrow 1\Uparrow$	$3\downarrow$	$1\Uparrow$	$\circ$	3.63	-3	1
$2\uparrow 1\Uparrow$	$\circ$	$1\Downarrow$	$1\uparrow$	3.64	3	3
$2\uparrow 1\Uparrow$	$3\downarrow$	$\circ$	$1\uparrow$	1.28	-1	1
$\circ$	$3\uparrow$	$1\Downarrow$	$1\uparrow$	1.96	5	3

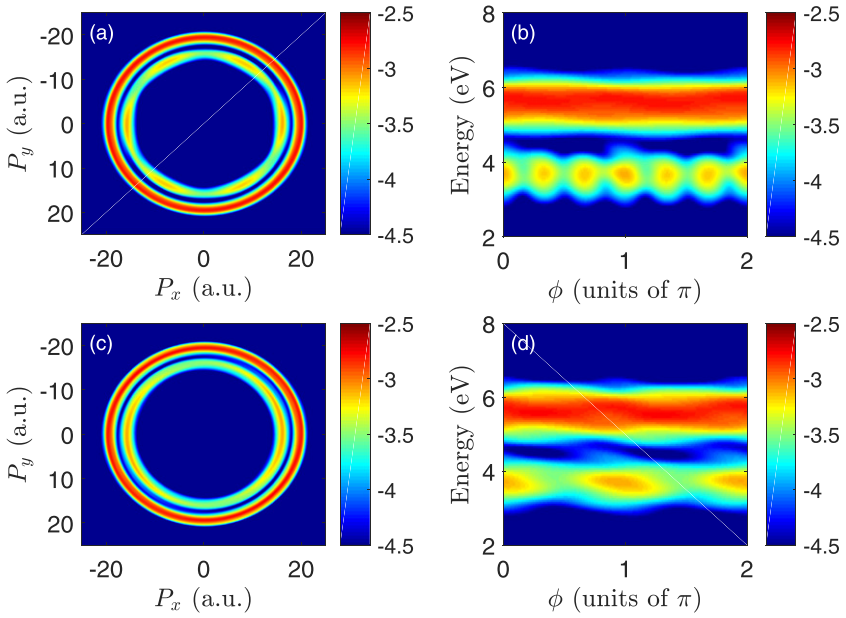

Figure 6. The two-dimension momentum distribution and angle-resolved KER distribution of H^+ fragments in the overlapped counter-rotating and co-rotating BiCP pulses with $\omega_1 : \omega_2 = 1 : 2$ are shown in (a), (b), (c) and (d), respectively. The wavelengths of $\mathbf{E}_1(t)$ and $\mathbf{E}_2(t)$ are 600 nm ($\omega_1 = 0.076$ a.u.) and 300 nm ($\omega_2 = 0.152$ a.u.), respectively. $L_1 = L_2 = 12.01$ fs. The intensity of $\mathbf{E}_1(t)$ and $\mathbf{E}_2(t)$ are 2.5×10^{13} W cm^{-2} and 7.5×10^{11} W cm^{-2}. The figures are logarithmic with the base of 10.

laser pulses, respectively. According to table 2, the fragments with the KER of 3.6 eV are from the $(2\uparrow 1\Uparrow, 3\downarrow, 1\uparrow, \circ)$ and $(2\uparrow 1\Uparrow, \circ, 1\Downarrow, 1\uparrow)$ pathways.

The simulated results starting from vibrational state $v = 1$, 2, 3 are shown in figure 7. And the result starting from coherent superimposed state are shown in figure 8. The symmetric structure with a period of $2\pi/6$ appears in these three results. The KER in the results are slightly higher than that predicted in table 2, because the KER in table 2 is obtained based on the ground vibrational state.

3.4. Weight yield of different pathways by wave packet interference

By comparing the interference patterns shown in figures 3(b) and 6(b), we found that the interference pattern in figure 3(b) has a higher contrast compared to that in figure 6(b). The contrast of interference pattern depends on the term $(|A_1(K)|^2 + |A_2(K)|^2 + 2A_1(K)A_2(K))/(|A_1(K)|^2 + |A_2(K)|^2 - 2A_1(K)A_2(K))$ in equation (6), which contain the information of the yield ratio of different dissociation pathways. If the fragment yields from the two pathways are close, the contrast of the interference fringes will be higher and, otherwise, the contrast will be lower. Therefore, we can estimate the yield ratio of different dissociation pathways by analyzing the contrast.

As an example, we will show how we can weigh the yield ratio between the $(2\uparrow 1\Uparrow, 3\downarrow, 1\uparrow, \circ)$ and $(2\uparrow 1\Uparrow, \circ, 1\Downarrow, 1\uparrow)$ pathways, the KER distributions of which are already shown in figure 6(b). The fragment yield with the KER of K can be represented by

$$\int_0^{2\pi} |A_1(K)|^2 + |A_2(K)|^2 + 2A_1(K)A_2(K)\cos(\Delta m\phi - \Delta\eta)\,\mathrm{d}\phi = \int_0^{2\pi} |A_1(K)|^2 \mathrm{d}\phi + \int_0^{2\pi} |A_2(K)|^2 \mathrm{d}\phi, \quad (7)$$

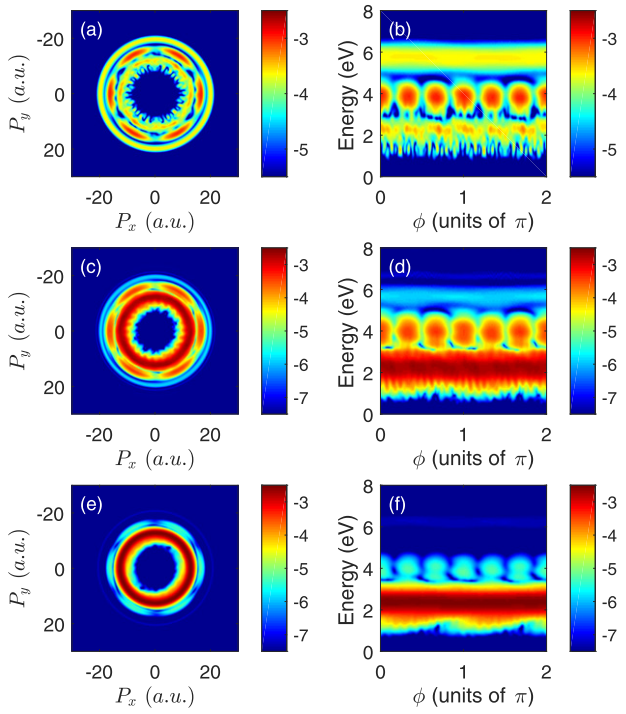

Figure 7. The two-dimension momentum distribution and angle-resolved KER distribution of H^+ fragments in the overlapped counter-rotating BiCP pulses with $\omega_1 : \omega_2 = 1{:}2$ starting from vibrational state $v = 2$, $v = 3$, $v = 4$ are shown in the first row, second row and third row, respectively. The wavelengths of $\mathbf{E}_1(t)$ and $\mathbf{E}_2(t)$ are 600 nm ($\omega_1 = 0.076$ a.u.) and 300 nm ($\omega_2 = 0.152$ a.u.), respectively. $L_1 = L_2 = 12.01$ fs. The intensity of $\mathbf{E}_1(t)$ and $\mathbf{E}_2(t)$ are 2.5×10^{13} W cm^{-2} and 2.5×10^{12} W cm^{-2}. The figures are logarithmic with the base of 10.

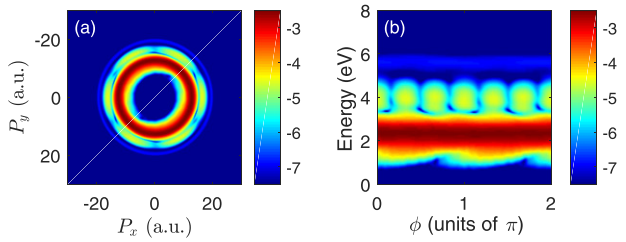

Figure 8. The two-dimension momentum distribution and angle-resolved KER distribution of H^+ fragments in the overlapped counter-rotating BiCP pulses with $\omega_1 : \omega_2 = 1{:}2$ starting from superimposed coherent state. The wavelengths of $\mathbf{E}_1(t)$ and $\mathbf{E}_2(t)$ are 600 nm ($\omega_1 = 0.076$ a.u.) and 300 nm ($\omega_2 = 0.152$ a.u.), respectively. $L_1 = L_2 = 12.01$ fs. The intensity of $\mathbf{E}_1(t)$ and $\mathbf{E}_2(t)$ are 2.5×10^{13} W cm^{-2} and 2.5×10^{12} W cm^{-2}. The figures are logarithmic with the base of 10.

where $\int_0^{2\pi}|A_1(K)|^2\mathrm{d}\phi$ and $\int_0^{2\pi}|A_2(K)|^2\mathrm{d}\phi$ represent the fragment yields from two pathways, respectively. The yield ratio of the two pathways can be represented by $|A_1(K')|^2/|A_2(K')|^2$. The angular distribution at KER $= K'$ is $|A_1(K')|^2 + |A_2(K')|^2 + 2A_1(K')A_2(K')\cos(\Delta m\phi - \Delta\eta)$, which can be obtained from the angle-resolved KER distributions. We take the angular distribution with KER $= K'$ and obtain an oscillating curve. The maxima and minima of the curve correspond to $(|A_1(K')|^2 + |A_2(K')|^2 + 2A_1(K')A_2(K'))$ and $(|A_1(K')|^2 + |A_2(K')|^2 - 2A_1(K')A_2(K'))$. We assume that the yield ratio is $|A_1(K')|^2/|A_2(K')|^2 = x : 1$. Then, we can obtain the yield ratio by solving the equation

$$\frac{x^2 + 1 + 2\sqrt{x}}{x^2 + 1 - 2\sqrt{x}} = \frac{|A_1(K')|^2 + |A_2(K')|^2 + 2A_1(K')A_2(K')}{|A_1(K')|^2 + |A_2(K')|^2 - 2A_1(K')A_2(K')}. \tag{8}$$

The angle-resolved KER distribution from 3.5 eV to 4 eV and the distribution with KER = 3.63 eV are shown in figures 9(a) and (b). We take the average of six local maxima (minima) as $(|A_1(K)|^2 + |A_2(K)|^2 + 2A_1(K)A_2(K))$ and $(|A_1(K)|^2 + |A_2(K)|^2 - 2A_1(K)A_2(K))$, respectively. By solving equation (8), We can obtain the yield ratio is $133 : 1$ at KER = 3.63 eV.

Using the angular distribution curve for different regions of the KER, we can obtain the yield ratios for each KER, which is shown in figure 9(c). We can see that the range of the yield ratios varies from about 110 to 240. So far, we are able to estimate the yield ratio between two interfering dissociation pathways. However, we have not yet determined which one of the two pathways dominates. In fact, we cannot simply determine the dominant pathway from the KER distributions, because $A_1(K)$ and $A_2(K)$ are interchangeable in equation (6) and they are indistinguishable from the observables shown in figure 9(a).

To identify which pathway dominates, we design a scheme based on the approach of wave packet interference. A third delayed CP laser pulse $\mathbf{E}_3(t)$ is introduced to generate the probe NWP, as shown in figure 9(d). The probe pulse $\mathbf{E}_3(t)$ is expressed as

$$\mathbf{E}_3(t) = \mathcal{E}_3[\cos(\omega_3(t - \Delta t))\hat{x} \pm \sin(\omega_3(t - \Delta t))\hat{y}] \times \sin^2\left(\frac{\pi(t - \Delta t)}{L_p}\right) \tag{9}$$

for $\Delta t < t < \Delta t + L_p$, where $\mathcal{E}_3$, ω_3, L_p are the field amplitude, angular frequency and the full duration of the probe pulse. Δt is the time delay for $\mathbf{E}_3(t)$. We have $\mathcal{E}_3 = 0.267$ a.u., $L_p = 8.01$ fs, $\omega_3 = 0.076$ a.u., and $\Delta t = 12$ fs in our calculation. Note that the delay Δt should not be too short, so that the probe pulse can be temporarily separated from the BiCP pulses. Different Δt will cause the slope of the interference stripes to be different in figure 9(e), which has been discussed in ionization studies [31, 32]. The given wavelength and pulse intensity of $\mathbf{E}_3(t)$ are used so that the KER of the probe NWP is approximately equal to 3.6 eV. In this case, the dissociation fragments driven by the probe pulse can interfere with the fragments from the $(2\uparrow 1\Uparrow, 3\downarrow, 1\uparrow, \circ)$ and $(2\uparrow 1\Uparrow, \circ, 1\Downarrow, 1\uparrow)$ pathways.

The interference structure contributed by the fragments from these three dissociation pathways in the angle-resolved KER distribution is according to

$$\begin{aligned}|\psi_1 + \psi_2 + \psi_3|^2 &= |A_1(K)\mathrm{e}^{\mathrm{i}[m_1\phi+\eta_1]} + A_2(K)\mathrm{e}^{\mathrm{i}[m_2\phi+\eta_2]} \\ &\quad + A_3(K)\mathrm{e}^{\mathrm{i}[m_3\phi+\eta_3]}|^2 \\ &= |A_1(K)|^2 + |A_2(K)|^2 + |A_3(K)|^2\end{aligned}$$

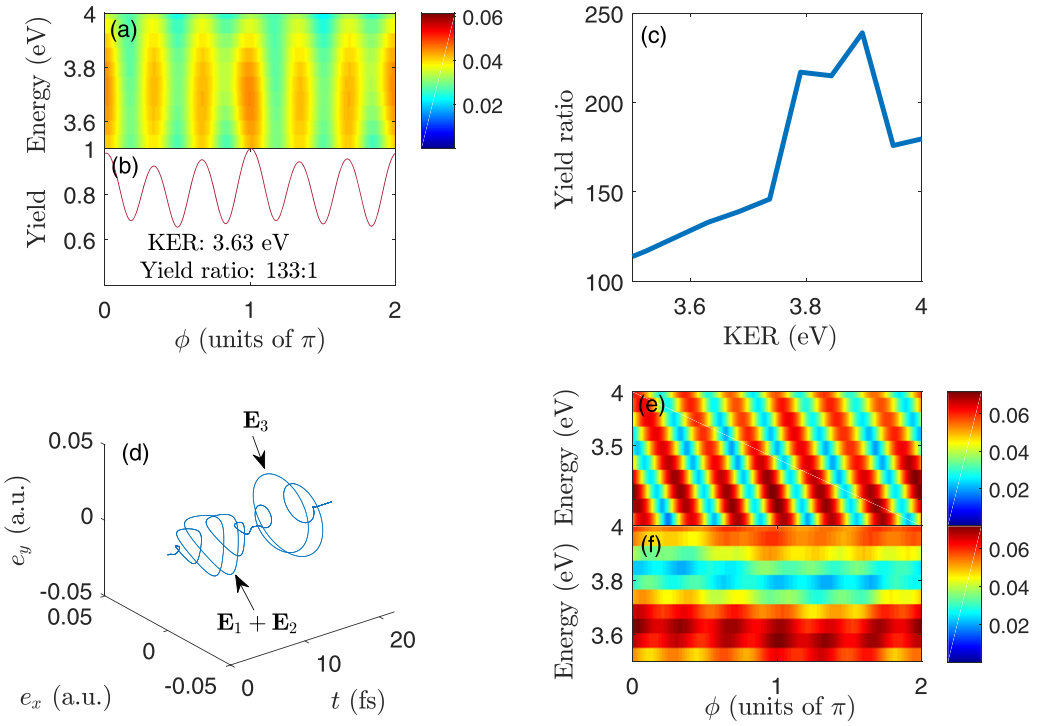

Figure 9. (a) Angle-resolved KER distribution with the KER range of 3.5 eV to 4 eV. (b) The distribution along ϕ with KER $= 3.63$ eV. (c) The yield ratio of the two pathways for different KER. (d) The electric field of the driving pulse and probe pulse. The delay of pulse peak between $\mathbf{E}_1(t) + \mathbf{E}_2(t)$ and $\mathbf{E}_3(t)$ is 12 fs. The interference pattern with left circularly probe pulse and right circularly probe pulse are shown in (e) and (f), respectively.

$$+ 2A_1(K)A_2(K)\cos(\Delta m_1\phi - \Delta\eta_1)$$
$$+ 2A_2(K)A_3(K)\cos(\Delta m_2\phi - \Delta\eta_2)$$
$$+ 2A_1(K)A_3(K)\cos(\Delta m_3\phi - \Delta\eta_3), \qquad (10)$$

where ψ_1 and ψ_2 represent the NWPs from $(2\uparrow 1\Uparrow, 3\downarrow, 1\uparrow, \circ)$ pathway and $(2\uparrow 1\Uparrow, \circ, 1\Downarrow, 1\uparrow)$ pathway, respectively. ψ_3 represents the probe NWP. m_1, m_2 and m_3 are angular momenta of ψ_1, ψ_2 and ψ_3. From table 2, we can obtain $m_1 = -3$ and $m_2 = +3$. We have $\Delta m_1 = m_1 - m_2$, $\Delta m_2 = m_2 - m_3$, and $\Delta m_3 = m_3 - m_1$, $\Delta\eta_1 = \eta_1 - \eta_2$, $\Delta\eta_2 = \eta_2 - \eta_3$, $\Delta\eta_3 = \eta_3 - \eta_1$.

From equation (10) we can see that interference patterns are contributed by the last three terms, which are interference of ψ_1 and ψ_2, ψ_2 and ψ_3, ψ_1 and ψ_3, respectively. We apply the probe pulse with right-rotating and left-rotating to generate ψ_3 in figures 9(e) and (f), respectively.

For the right-rotating probe pulse, m_3 is -3 and we have $\Delta m_2 = m_2 - m_3 = 6$ and $\Delta m_3 = m_1 - m_3 = 0$. Therefore, if ψ_2 dominates, the interference fringe of ψ_2 and ψ_3, whose period is $2\pi/6$, will be more pronounced. Conversely, if ψ_1 dominates, there will be no significant interference fringe, because $\Delta m_3 = 0$. For the left-rotating probe pulse, m_3 is $+3$. The situation is the exact opposite of the above.

In figure 9(e), the pronounced interference fringes with a period of $2\pi/6$ appear. And no significant interference fringes appear in figure 9(f). We therefore conclude that the NWP from $(2\uparrow 1\Uparrow, \circ, 1\Downarrow, 1\uparrow)$ pathway, namely ψ_2, is dominating.

4. Conclusion

In this study, we propose the MiPD pathway of H_2^+ in the BiCP pulses. The MiPD increases the variety of dissociation pathways, which have potential applications in manipulating chemical reactions. Using the MiPD, we can manipulate the angular distribution of ion fragments. By analyzing interference pattern, we can obtain rich information about the reaction pathway. We further propose a method based on wave packet interference, which can help us to weigh the dissociation fragments yield of different pathways but have the same KER. The method is essential to detect the MiPD.

Acknowledgments

This work is supported by the National Natural Science Foundation of China (Grant Nos. 92150106, 12174133, 11934006, 11627809, and 12021004) and the Open Fund of Hubei provincial Key Laboratory of Optical Information and Pattern Recognition (Grant No. 201902). The computing work in this paper

is supported by the Public Service Platform of High Performance Computing by Network and Computing Center of HUST.

Data availability statement

The data that support the findings of this study are available upon reasonable request from the authors.

ORCID iDs

Qingbin Zhang https://orcid.org/0000-0002-2277-7414

References

[1] Zewail A H 2000 *J. Phys. Chem.* A **104** 5660
[2] Weber T *et al* 2004 *Nature* **431** 437–40
[3] Bucksbaum P H, Zavriyev A, Muller H G and Schumacher D W 1990 *Phys. Rev. Lett.* **64** 1883
[4] Giusti-Suzor A, Mies F H, DiMauro L F, Charron E and Yang B 1995 *J. Phys. B: At. Mol. Opt. Phys.* **28** 309
[5] Calvert C R, Bryan W A, Newell W R and Williams I D 2010 *Phys. Rep.* **491** 1–28
[6] Roudnev V, Esry B D and Ben-Itzhak I 2004 *Phys. Rev. Lett.* **93** 163601
[7] Sändig K, Figger H and Hänsch T W 2000 *Phys. Rev. Lett.* **85** 4876
[8] Nabekawa Y, Furukawa Y, Okino T, Amani Eilanlou A, Takahashi E J, Yamanouchi K and Midorikawa K 2016 *Nat. Commun.* **7** 12835
[9] Kling M F *et al* 2006 *Science* **312** 155m
[10] Xu T and He F 2014 *Phys. Rev.* A **90** 053401
[11] Li H, Gong X, Lin K, de Vivie-Riedle R, Tong X M, Wu J and Kling M F 2017 *J. Phys. B: At. Mol. Opt. Phys.* **50** 172001
[12] Znakovskaya I *et al* 2012 *Phys. Rev. Lett.* **108** 063002
[13] Chen Z and He F 2020 *Phys. Rev.* A **102** 033107
[14] Chen Z, He P L and He F 2020 *Phys. Rev.* A **101** 033406
[15] Lin K *et al* 2016 *J. Phys. B: At. Mol. Opt. Phys.* **49** 025603
[16] Ngoko Djiokap J M, Meremianin A V, Manakov N L, Hu S X, Madsen L B and Starace Anthony F 2016 *Phys. Rev.* A **94** 013408
[17] Zhen Q, Zhang S Q, Yang Z J and Liu X S 2021 *Europhys. Lett.* **133** 33001
[18] Yuan K-J and Bandrauk A D 2018 *J. Phys. Chem.* A **122** 2241
[19] Hu C and He F 2021 *Phys. Rev.* A **104** 063107
[20] Anis F and Esry B D 2012 *Phys. Rev. Lett.* **109** 133001
[21] Tal-Ezer H and Kosloff R 1986 *Chem. Phys. Lett* **127** 223
[22] Xu H, Hu H, Tong X M, Liu P, Li R, Sang Robert T and Litvinyuk Igor V 2016 *Phys. Rev.* A **93** 063416
[23] He F and Thumm U 2010 *Phys. Rev.* A **81** 053413
[24] Gong X, He P, Song Q, Ji Q, Pan H, Ding J, He F, Zeng H and Wu J 2014 *Phys. Rev. Lett.* **113** 203001
[25] He F, Ruiz C and Becker A 2007 *Phys. Rev. Lett.* **99** 083002
[26] Kremer M *et al* 2009 *Phys. Rev. Lett.* **103** 213003
[27] Liu K, Zhang Q and Lu P 2012 *Phys. Rev.* A **86** 033410
[28] Eppink A T J B and Parker D H 1997 *Rev. Sci. Instrum.* **68** 3477
[29] Lin J J, Zhou J, Shiu W and Liu K 2003 *Rev. Sci. Instrum.* **74** 2495
[30] Dörner R, Mergel V, Jagutzki O, Spielberger L, Ullrich J, Moshammer R and Schmidt-Böcking H 2000 *Phys. Rep.* **330** 95
[31] Ngoko Djiokap J M, Hu S X, Madsen L B, Manakov N L, Meremianin A V and Starace A F 2015 *Phys. Rev. Lett.* **115** 113004
[32] Pengel D, Kerbstadt S, Englert L, Bayer T and Wollenhaupt M 2017 *Phys. Rev.* A **96** 043426